INTERNATIONAL JOURNAL FOR NUMERICAL METHODS IN FLUIDS
Int. J. Numer. Meth. Fluids **26**: 851–874 (1998)

SIMULATION OF PARTICLE SETTLING IN ROTATING AND NON-ROTATING FLOWS OF NON-NEWTONIAN FLUIDS

P. RAMESHWARAN, P. TOWNSEND AND M.F. WEBSTER*

University of Wales Institute of non-Newtonian Fluid Mechanics, Department of Computer Science, University of Wales Swansea, Swansea, SA2 8PP, UK

SUMMARY

Finite element solutions are presented for the flow of Newtonian and non-Newtonian fluids around a sphere falling along the centreline of a cylindrical tube. Both rotating and stationary tube scenarios are considered. Calculations are reported for three different inelastic constitutive models that manifest shear-thinning, extension-thickening and their combination. The influence of inertia and these various forms of viscous response are examined for their influence upon the drag on the settling particle and the structure of the flow. Simulations are performed by employing a semi-implicit time marching Taylor–Galerkin/pressure-correction finite element algorithm, a fractional-staged scheme of second-order-accuracy. © 1998 John Wiley & Sons, Ltd.

KEY WORDS: finite elements; Taylor–Galerkin/pressure correction; particle settling; drag; rotating and non-rotating flows; inelastic non-Newtonian fluids

1. INTRODUCTION

The presence and motion of particles in Newtonian or non-Newtonian fluids is ubiquitous. They are of fundamental importance in many natural and physical processes and in a large number of industrial applications such as chemical, genetic and biomedical engineering processes. Over the past three decades, there has been an increasing recognition of the non-Newtonian flow characteristics displayed by many common materials. The study of the behaviour of settling particles in a fluid medium has been a classical problem in fluid mechanics and in rheology. Of the theoretical, experimental and numerical studies available in the literature the majority deal with Newtonian fluids [1,2]. Conversely, for non-Newtonian fluids the problem is considerably more complex and the analysis depends on the particular fluid model adopted [3].

One practical problem is to determine the rate of settling of particles. Such knowledge is particularly significant in determining, e.g. the shelf life of materials such as foodstuffs, cleaning materials and many others. Also, in oil and gas drilling it is important to understand the distribution of loose material, removed by the drill bit and carried to the surface by the drilling mud. Concentrations of such material can have catastrophic consequences, causing failure in the drilling operation and incurring vast expense [1–3].

* Correspondence to: University of Wales Institute of non-Newtonian Fluid Mechanics, Department of Computer Science, University of Wales Swansea, Swansea, SA2 8PP, UK.

CCC 0271–2091/98/070851–24$17.50

Received January 1997
Revised June 1997

It is well-recognised that extensional behaviour in non-Newtonian fluids plays a major role in complex flows. Most non-Newtonian fluids, such as polymeric solutions and melts, exhibit shear-thinning and extension-thickening behaviour [4,5]. However, it is not straightforward to segregate extensional and shear properties within the constitutive modelling as they are intimately related. In the present study, consideration is given to the behaviour of a class of generalised Newtonian fluids which, in three-dimensional flows, exhibit shear and extensional behaviour, whilst being dissociated from the complications of memory effects. The inelastic viscosity is prescribed as a function of the second and third invariant of the rate of deformation tensor [6].

The motion of a spherical particle falling along the centreline of a stationary cylindrical tube has received much attention as a benchmark problem over the last decade, with particular interest in the effect of surrounding container walls on the rate of settling. The underlying theory is well established for Newtonian fluids; for non-Newtonian flows, the problem is more challenging. The drag coefficient or wall correction factor on the sphere can either increase or decrease, depending on the precise model chosen. For Newtonian fluids, exact and approximate theoretical solutions have been given by Bohlin [7], and Haberman and Sayre [8]. Fayon and Happel [9] gave a semi-empirical equation for the drag coefficient as a function of Reynolds number. Theoretical and experimental results on associated pressure drops have been reported by Feldman and Brenner [10]. Analytical solutions for Newtonian fluids are available to calibrate numerical solutions and to determine their accuracy. Extension into the non-Newtonian regime is the ensuing challenge.

Theoretical solutions for the slow flow of an inelastic fluid past a sphere are available in the literature, e.g. those cited by Kawase and Moo-Young [11]. Experimental results on the problem include the works of Oh and Lee [12] and Chhabra and Uhlherr [13]. Non-Newtonian numerical results are attributed as follows: finite element results (FEM) of Gu Dazhi and Tanner [14] and Graham and Jones [15] for a power-law model, and Debbaut and Crochet [6] and Oh and Lee [12] for a shear and extension-rate dependent model. Also, boundary element results (BEM) have been reported by Bush and Phan-Thien [16] and Zheng *et al*. [17] for a Carreau model. The drag coefficient induced on the falling sphere in a viscoelastic flow has been studied extensively and a comprehensive survey is reported on the matter by Chhabra [3].

The corresponding rotating flow has also been the subject of several theoretical and experimental investigations, such as that given by Taylor [18] for unbounded Newtonian flows. These flows are characterised by a Taylor number, $Ta = \rho\omega a^2/\mu_o$, Reynolds number, $Re = \rho V_s a/\mu_o$ and Rossby number, $R_o = V_s/\omega a = Re/Ta$, where a is the sphere radius, V_s is the sphere velocity, ω is the solid body rotation rate, ρ is the fluid density and, μ_o is the viscosity. Taylor showed that a slowly translating sphere in a rotating fluid is accompanied by a fluid column parallel to the rotating axis. Inside this column the fluid was pushed along in front of the sphere. These 'Taylor columns' form in an unbounded fluid when the convective acceleration is small. Pritchard [19] showed that a Taylor column appears in an unbounded fluid when the Rossby number is less than 0.7.

The drag force on the falling sphere has complicated dependency on the sphere velocity and the solid body angular rotation. Maxworthy [20] has measured the drag for small Reynolds and Taylor numbers in both the bounded (with small sphere to cylinder radius ratio) and unbounded instances. Most of the theoretical results in the literature are for unbounded Newtonian flows. For unbounded rotating flows, the first attempt to solve an initial-value problem for an inviscid fluid was that by Grace [21]. Subsequently, Stewartson [22] derived an exact expression. Childress [23] studied the viscous problem for very small Reynolds and Taylor numbers, and determined a first correction to the Stokes drag. Weisenborn [24] used the

method of induced forces to determine the drag for an arbitrary Taylor number. More recently, Tanzosh and Stone [25] have presented theoretical and numerical results for the viscous case. Dennis *et al.* [26] calculated the drag numerically for small Taylor and Reynolds numbers. A theoretical solution is available for unbounded rotating Newtonian flow [22–25]. However, for bounded rotating flows, the problem defies analytic solution and demands numerical resolution.

The objective of the present study is to conduct numerical simulations for the settling of particles in either Newtonian or non-Newtonian fluids, considering both the rotating and non-rotating surrounding cylinder problems. A variety of constitutive models are considered, including Newtonian, shear-thinning, extension-thickening and combined shear-thinning and extension-thickening formulations. The influence of inertia and viscosity on the drag and the structure of the flow are investigated in some detail. The present work employs a Taylor–Galerkin finite element method to analyse the problem, in combination with a fractional-staged projection method. This employs a semi-implicit time stepping scheme, prior to a spatial Galerkin discretisation that is both stable and second-order-accurate. Both direct and iterative solvers are invoked, and an element-wise approach is adopted to circumvent the difficulty of dealing directly with a complete system matrix. The algorithm is described in extensive detail in Hawken *et al.* [27].

2. GOVERNING EQUATIONS

2.1. Equations of motion

A cylindrical co-ordinate system (r, θ, z) is appropriate to define the problem, assuming axisymmetry. Without loss of generality, the problem statement is presented for the rotating instance, the non-rotating case being a straightforward simplification. Non-dimensional variables and scales are introduced as

$$r^* = \frac{r}{L}, \quad z^* = \frac{z}{L}, \quad v_r^* = \frac{v_r}{V}, \quad v_\theta^* = \frac{v_\theta}{V},$$
$$v_z^* = \frac{v_z}{V}, \quad p^* = \frac{pL}{V\mu_o}, \quad t^* = \frac{t\mu_o}{L^2\rho}, \quad \mu^* = \frac{\mu}{\mu_o},$$

where t represents time, L a characteristic length (sphere radius a), V a characteristic velocity (sphere velocity, V_s) and μ_o a constant reference viscosity. Fluid parameters are velocity $\boldsymbol{v} = (v_r, v_\theta, v_z)$, pressure p, density ρ and viscosity μ. For brevity, * notation is elected by implication. Under isothermal conditions, the non-dimensional equations that describe the steady motion of a falling sphere in an incompressible inelastic fluid, along the centreline of a rotating cylindrical tube of infinite length, are

$$\frac{\partial v_r}{\partial r} + \frac{v_r}{r} + \frac{\partial v_z}{\partial z} = 0, \tag{1}$$

$$\frac{\partial v_r}{\partial t} = \left\{\frac{1}{r}\frac{\partial}{\partial r}\left(2\mu r \frac{\partial v_r}{\partial r}\right) - 2\mu\frac{v_r}{r^2} + \frac{\partial}{\partial z}\left[\mu\left(\frac{\partial v_z}{\partial r} + \frac{\partial v_r}{\partial z}\right)\right]\right\} - Re\left(v_r\frac{\partial v_r}{\partial r} - \frac{v_\theta^2}{r} + v_z\frac{\partial v_r}{\partial z}\right) - \frac{\partial p}{\partial r}, \tag{2a}$$

$$\frac{\partial v_\theta}{\partial t} = \left\{\frac{1}{r^2}\frac{\partial}{\partial r}\left[\mu r^3 \frac{\partial}{\partial r}\left(\frac{v_\theta}{r}\right)\right] + \frac{\partial}{\partial z}\left(\mu \frac{\partial v_\theta}{\partial z}\right)\right\} - Re\left(v_r \frac{\partial v_\theta}{\partial r} + \frac{v_r v_\theta}{r} + v_z \frac{\partial v_\theta}{\partial z}\right), \tag{2b}$$

$$\frac{\partial v_z}{\partial t} = \left\{\frac{1}{r}\frac{\partial}{\partial r}\left[\mu r \left(\frac{\partial v_z}{\partial r} + \frac{\partial v_r}{\partial z}\right)\right] + \frac{\partial}{\partial z}\left(2\mu \frac{\partial v_z}{\partial z}\right)\right\} - Re\left(v_r \frac{\partial v_z}{\partial r} + v_z \frac{\partial v_z}{\partial z}\right) - \frac{\partial p}{\partial r}. \tag{2c}$$

In the non-rotating case, the azimuthal velocity component vanishes and Equation (2b) is trivially satisfied.

2.2. Constitutive equations

Most non-Newtonian fluids in steady shear exhibit shear-thinning behaviour. Alternatively, in steady extension many fluids display a viscosity that increases with an increase in extension rate. There has been significant interest expressed in identifying a simple constitutive equation that will adequately account for both shear and extensional response [6,12,28]. Some viscoelastic constitutive equations can account for both shear-thinning and extension-thickening behaviour [5]. However, such models are encumbered by material memory that complicates the analysis and prediction. An inelastic constitutive equation is adopted here to model this mixed shear and extension regime. Three constitutive models are chosen, namely a shear-thinning model and an extension-thickening model of Debbaut and Crochet [6], and a combined shear-thinning and extension-thickening model. These models allow the investigation of the effects of shear and extensional viscosity independently, and in their combination, being defined as

$$\text{Model 1:} \quad \mu(\dot\gamma) = [1 + (We\dot\gamma)^2]^{(n-1)/2}, \tag{3a}$$

$$\text{Model 2:} \quad \mu(\dot\varepsilon) = \cosh(mWe\dot\varepsilon), \tag{3b}$$

$$\text{Model 3:} \quad \mu(\dot\gamma, \dot\varepsilon) = [1 + (We\dot\gamma)^2]^{(n-1)/2} \cosh(mWe\dot\varepsilon), \tag{3c}$$

where n is a power-law index, m is a material constant, $\dot\gamma$ is a shear rate and $\dot\varepsilon$ an extension rate. The non-dimensional number We is

$$We = \frac{\lambda V}{L}, \tag{4}$$

where λ is a time constant. The shear rate and extension rate are defined by the second invariant, $II_D = (1/2)\, tr(D^2)$ and third invariant, $III_D = \det D$, of the rate of deformation tensor, $D = 1/2(\nabla \boldsymbol{v} + \nabla \boldsymbol{v}^T)$, via

$$\dot\gamma = 2\sqrt{II_D}, \tag{5}$$

$$\dot\varepsilon = \frac{3III_D}{II_D}. \tag{6}$$

For an axisymmetric rotating flow, the second and third invariant of the rate of deformation tensor are given as

$$D = \begin{bmatrix} \dfrac{\partial v_r}{\partial r} & \dfrac{1}{2}\left[r \dfrac{\partial}{\partial r}\left(\dfrac{v_\theta}{r}\right)\right] & \dfrac{1}{2}\left(\dfrac{\partial v_z}{\partial r} + \dfrac{\partial v_r}{\partial z}\right) \\ \dfrac{1}{2}\left[r \dfrac{\partial}{\partial r}\left(\dfrac{v_\theta}{r}\right)\right] & \dfrac{v_r}{r} & \dfrac{1}{2}\left(\dfrac{\partial v_\theta}{\partial z}\right) \\ \dfrac{1}{2}\left(\dfrac{\partial v_z}{\partial r} + \dfrac{\partial v_r}{\partial z}\right) & \dfrac{1}{2}\left(\dfrac{\partial v_\theta}{\partial z}\right) & \dfrac{\partial v_z}{\partial z} \end{bmatrix}, \tag{7}$$

$$II_D = \frac{1}{2}\left\{\left(\frac{\partial v_r}{\partial r}\right)^2 + \left(\frac{\partial v_z}{\partial z}\right)^2 + \left(\frac{v_r}{r}\right)^2 + \frac{1}{2}\left(\frac{\partial v_\theta}{\partial z}\right)^2 + \frac{1}{2}\left[r \frac{\partial}{\partial r}\left(\frac{v_\theta}{r}\right)\right]^2 + \frac{1}{2}\left(\frac{\partial v_z}{\partial r} + \frac{\partial v_r}{\partial z}\right)^2\right\}, \tag{8}$$

$$III_D = \frac{v_r}{r}\frac{\partial v_r}{\partial r}\frac{\partial v_z}{\partial z} - \frac{1}{4}\frac{\partial v_r}{\partial r}\left(\frac{\partial v_\theta}{\partial z}\right)^2 - \frac{1}{4}\frac{\partial v_z}{\partial z}\left[r \frac{\partial}{\partial r}\left(\frac{v_\theta}{r}\right)\right]^2 + \frac{1}{4}\frac{\partial v_\theta}{\partial z}\left(\frac{\partial v_z}{\partial r} + \frac{\partial v_r}{\partial z}\right)\left[r \frac{\partial}{\partial r}\left(\frac{v_\theta}{r}\right)\right] - \frac{1}{4}\frac{v_r}{r}\left(\frac{\partial v_z}{\partial r} + \frac{\partial v_r}{\partial z}\right)^2. \tag{9}$$

3. NUMERICAL ALGORITHM

3.1. Discretisation of the system

A semi-implicit version of the Taylor–Galerkin–pressure-correction finite element discretisation has been employed in this study for primary solution variables of velocity and pressure. A full description of the numerical scheme is provided in Hawken *et al.* [27]. A temporal discretisation in a Taylor series expansion is performed before a spatial Galerkin discretisation, to extract the time stepping scheme. The method adopts a Lax–Wendroff approach, revisited in the finite element context. The pressure-correction scheme is a fractional step method that is employed to resolve the incompressibility constraint. This scheme is compatible with a Taylor–Galerkin implementation, guaranteeing second-order-accuracy and stability. Combining a pressure correction scheme for temporal increment on pressure with a predictor-corrector Taylor–Galerkin scheme, provides the basis for the present second-order numerical scheme. In a semi-implicit formulation, the diffusion term is treated implicitly in a Crank–Nicolson manner, whilst convection terms are treated explicitly. This choice removes a diffusive stability restriction that would result from a fully explicit time stepping scheme.

The various fractional stages are described as follows. At a first fractional stage a non-solenoidal velocity field is computed using a half time-step, and a predictor-corrector scheme over the full time-step. In the first half time-step $(n+1/2)$, the predictor, the velocity is computed from data at time level (n); while in a second half time-step, the corrector, the solutions at time steps (n) and $(n+1/2)$ are used to calculate an intermediate non-solenoidal velocity field. Subsequently at a second stage, a Poisson equation for the difference in pressure over the time step is determined. At a third and final stage a solenoidal velocity field is evaluated as a correction, based on the temporal pressure difference. This completes a time step cycle. The system of equations at step one and three are governed by mass matrices resulting from discretisation of time derivatives. These are solved using iterative methods. At step two, the pressure stiffness matrix equation is solved directly using a Choleski method. In the Galerkin spatial discretisation, piecewise continuous quadratic (ϕ) and linear (ψ) functions are employed to approximate the velocity components, $\boldsymbol{V}(\boldsymbol{x}, t)$, and pressure, $\boldsymbol{P}(\boldsymbol{x}, t)$, respectively, over triangular subdivisions of the domain as

$$\boldsymbol{V}(\boldsymbol{x}, t) = \boldsymbol{V}_j(t)\phi_j(\boldsymbol{x}), \qquad \boldsymbol{P}(\boldsymbol{x}, t) = \boldsymbol{P}_l(t)\psi_l(\boldsymbol{x}). \tag{10}$$

The fully discrete equation system is represented as
Step 1a:

$$\left(\frac{2}{\Delta t}\boldsymbol{M} + \frac{1}{2}\boldsymbol{S}\right)(\boldsymbol{V}^{n+(1/2)} - \boldsymbol{V}^n) = \frac{1}{2}(\boldsymbol{F}^{n+(1/2)} + \boldsymbol{F}^n) + [-\boldsymbol{S}\boldsymbol{V} - (Re)\boldsymbol{N}(\boldsymbol{V}) + \boldsymbol{L}^T\boldsymbol{P}]^n, \tag{11a}$$

Step 1b:

$$\left(\frac{1}{\Delta t}\boldsymbol{M} + \frac{1}{2}\boldsymbol{S}\right)(\boldsymbol{V}^* - \boldsymbol{V}^n) = \frac{1}{2}(\boldsymbol{F}^{n+1} + \boldsymbol{F}^n) + (-\boldsymbol{S}\boldsymbol{V} + \boldsymbol{L}^T\boldsymbol{P})^n - [(Re)\boldsymbol{N}(\boldsymbol{V})]^{n+(1/2)}, \tag{11b}$$

Step 2:

$$\theta\boldsymbol{K}\boldsymbol{Q}^{n+1} = -\frac{1}{\Delta t}\boldsymbol{L}\boldsymbol{V}^*, \tag{11c}$$

Step 3:

$$\frac{1}{\Delta t}\boldsymbol{M}(\boldsymbol{V}^{n+1} - \boldsymbol{V}^*) = \theta\boldsymbol{L}^T\boldsymbol{Q}^{n+1}, \tag{11d}$$

where n is a time step index, $\boldsymbol{V}^n$ is a nodal velocity vector at time t^n, $\boldsymbol{V}^*$ is an intermediate non-solenoidal velocity vector, $\boldsymbol{P}$ is a pressure vector at time t^n, $\boldsymbol{Q}^{n+1} = \boldsymbol{P}^{n+1} - \boldsymbol{P}^n$, $\boldsymbol{F}^n$ is a forcing function vector due to boundary conditions at time t^n, $\boldsymbol{M}$ is a consistent mass matrix, $\boldsymbol{S}$ is a momentum diffusion matrix, $\boldsymbol{N}(\boldsymbol{V})$ is a convection matrix, $\boldsymbol{L}$ is a divergence/pressure gradient matrix, $\boldsymbol{K}$ is a pressure stiffness matrix and θ is the time stepping splitting factor on the pressure gradient terms. The system matrices are defined as

$$\boldsymbol{M}_{ij} = \int_\Omega \phi_i\phi_j r \, \mathrm{d}\Omega,$$

$$\boldsymbol{S}_{ij} = \begin{bmatrix} S_{rr} & 0 & S_{rz} \\ 0 & S_{\theta\theta} & 0 \\ S_{zr} & 0 & S_{zz} \end{bmatrix}_{ij},$$

where

$$(S_{rr})_{ij} = \int_\Omega \mu\left(2\frac{\partial\phi_i}{\partial r}\frac{\partial\phi_j}{\partial r} + \frac{\partial\phi_i}{\partial z}\frac{\partial\phi_j}{\partial z} + 2\frac{\phi_i\phi_j}{r^2}\right)r \, \mathrm{d}\Omega,$$

$$(S_{rz})_{ij} = \int_\Omega \mu\left(\frac{\partial\phi_i}{\partial r}\frac{\partial\phi_j}{\partial z}\right)r \, \mathrm{d}\Omega = (S_{rz})_{ij}^T,$$

$$(S_{\theta\theta})_{ij} = \int_\Omega \mu\left(\frac{\partial\phi_i}{\partial r}\frac{\partial\phi_j}{\partial r} + \frac{\partial\phi_i}{\partial z}\frac{\partial\phi_j}{\partial z} + \frac{\phi_i\phi_j}{r^2}\right)r \, \mathrm{d}\Omega,$$

$$\boldsymbol{N}_{ij}(\boldsymbol{V}) = \begin{bmatrix} N(V)_r \\ N(V)_\theta \\ N(V)_z \end{bmatrix}_{ij},$$

where

$$[N(V)_r]_{ij} = \int_\Omega \left(\phi_l v_r^l \frac{\partial \phi_j}{\partial r} v_r^j - \frac{\phi_l v_\theta^l \phi_j v_\theta^j}{r} + \phi_l v_z^l \frac{\partial \phi_j}{\partial z} v_r^j \right) \phi_i r \, \mathrm{d}\Omega,$$

$$[N(V)_\theta]_{ij} = \int_\Omega \left(\phi_l v_r^l \frac{\partial \phi_j}{\partial r} v_\theta^j + \frac{\phi_l v_r^l \phi_j v_\theta^j}{r} + \phi_l v_z^l \frac{\partial \phi_j}{\partial z} v_\theta^j \right) \phi_i r \, \mathrm{d}\Omega,$$

$$[N(V)_z]_{ij} = \int_\Omega \left(\phi_l v_r^l \frac{\partial \phi_j}{\partial r} v_z^j + \phi_l v_z^l \frac{\partial \phi_j}{\partial z} v_z^j \right) \phi_i r \, \mathrm{d}\Omega,$$

$$\boldsymbol{L}_{ij} = [L_r \quad 0 \quad L_z]_{il},$$

where

$$(L_r)_{il} = \int_\Omega \left(\frac{\partial \phi_i}{\partial r} + \frac{\phi_i}{r} \right) \psi_l r \, \mathrm{d}\Omega,$$

$$(L_z)_{il} = \int_\Omega \frac{\partial \phi_i}{\partial z} \psi_l r \, \mathrm{d}\Omega,$$

$$\boldsymbol{K}_{ij} = \int_\Omega \left(\frac{\partial \psi_k}{\partial r} \frac{\partial \psi_l}{\partial r} + \frac{\partial \psi_k}{\partial z} \frac{\partial \psi_l}{\partial z} \right) r \, \mathrm{d}\Omega.$$

Repeated indices imply summation taken over i and j for all velocity nodal points, and k and l for all vertex pressure nodal points on the triangular meshes. For second-order-accuracy in time, the Crank–Nicolson choice of $\theta = 0.5$ is adopted. The forcing vector $\boldsymbol{F}$ vanishes identically, as there are no body forces acting.

3.2. Drag on the sphere

A Taylor–Galerkin finite element solution provides nodal values for both the velocity and pressure. Drag coefficient calculations involve the gradients of these primary variables. Gradients are discontinuous on the domain and must be postprocessed from the relevant fields to yield continuous representations. Levine [29] has shown that the average of the normal derivatives on either side of a triangle edge are superconvergent (gradient of greater accuracy within an element) at midpoints of the element. The existence of superconvergent points at midpoints of the element sides is of significance in the direct recovery method used here. Non-unique values are recorded at the nodal points at each midside node in adjoining elements. The values of the gradients are calculated by averaging at the midside nodes. Gradients at vertex nodes are calculated by averaging the nodal gradient contributions in elements which share that node. The advantage of the direct recovery method is the superior accuracy it may access, reliant on the superconvergent properties available. Further details on this direct method can be found in Hawken *et al.* [30].

The dimensionless drag force on a moving sphere is evaluated by integrating the pressure and stresses over the sphere surface that may be represented as

$$D = 2\pi a^2 \int_0^\pi \left[\mu \left(\frac{\partial v_z}{\partial r} + \frac{\partial v_r}{\partial z} \right) \sin\theta + \left(-p + 2\mu \frac{\partial v_z}{\partial z} \right) \cos\theta \right] \sin\theta \, \mathrm{d}\theta. \tag{12}$$

The so-called Stokes drag force on a sphere falling in an unbounded Newtonian fluid is given by

$$D_\infty = 6\pi\mu a V_s. \tag{13}$$

The wall correction factor or drag coefficient of a sphere falling in a bounded fluid is defined through

$$K = \frac{D}{D_\infty}. \tag{14}$$

4. PROBLEM SPECIFICATION

The problem is illustrated schematically in Figure 1. The cylindrical tube rotates about the z-axis at rotation rate ω and moves past the sphere at velocity V_s. In the stationary cylinder case, ω vanishes. The sphere to cylinder radius ratios, a/R of 0.5 and 0.2 are chosen to illustrate the influence of different geometric ratios.

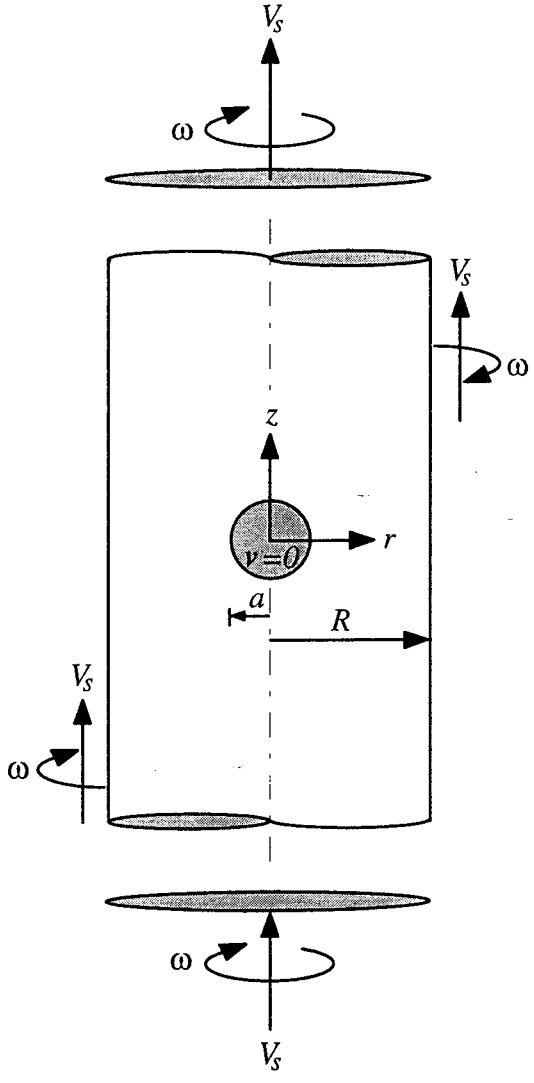

Figure 1. Schematic diagram of a sphere falling through a rotating fluid in a cylinder.

Table I. Summary of finite element meshes, $a/R = 0.5$

Mesh	Sphere surface nodes	Elements	Nodes
M1	11	400	891
M2	21	1600	3381
M4	41	6400	13 161

The non-linearity of the system of equations and the formation of steep velocity and stress gradients around the sphere surface render numerical calculations for flows with inertial and non-Newtonian behaviour more difficult than for their low Reynolds number Newtonian flow counterparts. Sufficiently large upstream and downstream cylinder lengths are selected in order to sustain fully developed entry and exit flow and avoid end effects. For both geometric ratios selected, the upstream length is equal to the downstream length, taken as $40a$ for $a/R = 0.5$ and $20a$ for $a/R = 0.2$. These specifications are chosen by empirical investigation to satisfy fully developed flow to within O(0.01%).

For $a/R = 0.5$, the flow domain is meshed by employing non-uniform conformal mapping, a technique which automatically aligns element sides with streamlines. In this case, three structured finite element meshes are used, as listed in Table I and shown in Figure 2. Meshes

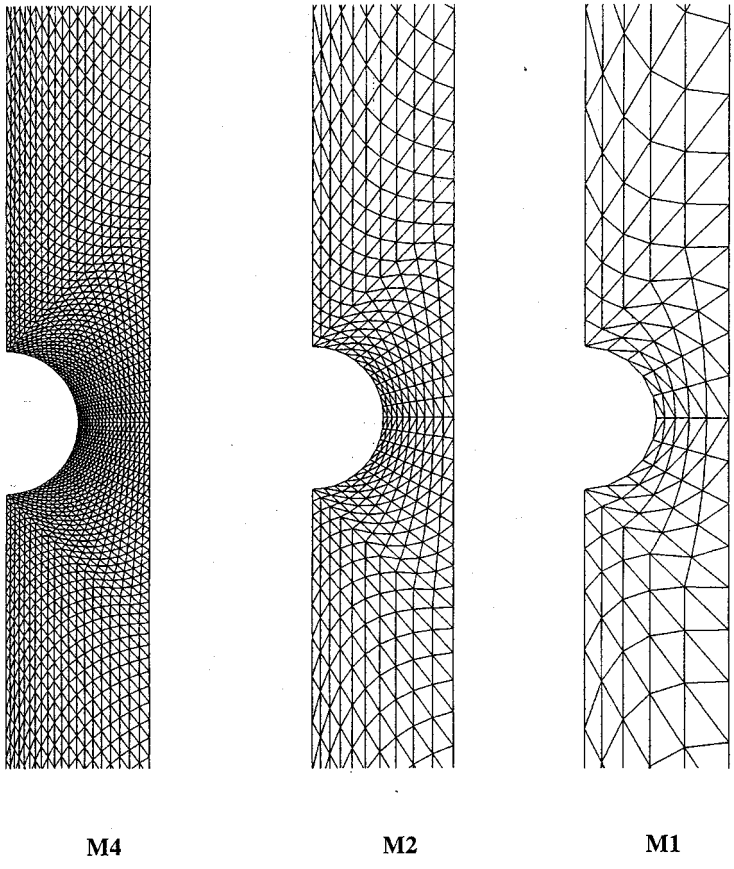

Figure 2. Mesh patterns around sphere, $a/R = 0.5$.

Table II. Summary of finite element meshes, $a/R = 0.2$

Mesh	Sphere surface nodes	Elements	Nodes
AM1	21	644	1401
AM2	31	948	2035
AM3	41	1242	2645

M2 and M4 are hierarchical h-refinements of M1 and M2 respectively, where each triangular parent element is divided into four elements by connecting the midside nodes of parent elements. The order of approach adopted was first to analyse the case of $a/R = 0.5$ with a structured mesh option. When the wider gap scenario of $a/R = 0.2$ was subsequently considered, it became apparent that a more localised treatment through unstructured meshing was preferential, essentially to capture the flow phenomena more tightly in the vicinity of the

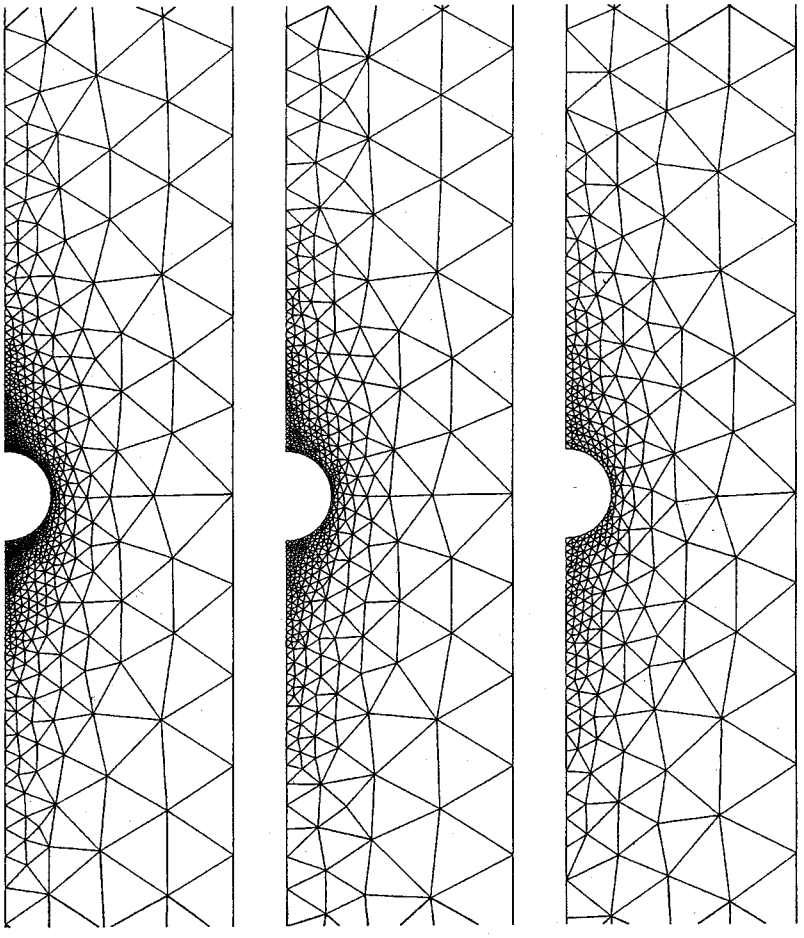

Figure 3. Mesh patterns around sphere, $a/R = 0.2$.

sphere surface where most activity occurs. Unstructured meshes are more flexible, introducing localised spatial resolution where necessary, and are more economical in run time. For $a/R = 0.2$, three unstructured meshes, AM1, AM2 and AM3, are generated by an adaptive mesh generator, as given in Table II and shown in Figure 3. In each case, the flow domain is meshed with a fine mesh in the vicinity of stagnation points and sphere surface, while using coarser meshing elsewhere. The grading of meshes is employed to confirm solution accuracy through mesh refinement.

For any chosen value of the Reynolds number, computation commences from quiescent initial conditions. Subsequently, for each value of a particular parameter space explored, the time-stepping procedure is accelerated by adopting prior value steady state solutions as start-up conditions. A relative increment time-stepping termination tolerance is selected of the order of 10^{-6} to detect convergence to a steady state. The following boundary conditions apply for the rotating cylinder problem

At the inlet of the flow: $v_r = 0$, $v_\theta = r\omega$ and $v_z = V_s$,
Along the cylindrical tube ($r = R$): $v_r = 0$, $v_\theta = R\omega$ and $v_z = V_s$,
Along the centreline of the cylindrical tube ($r = 0$): $v_r = 0$, $v_\theta = 0$ and $\partial v_z/\partial r = 0$,
On the surface of the sphere: $v_r = v_\theta = v_z = 0$,
At the outlet of the flow: $v_r = 0$, $v_\theta = r\omega$, $\partial v_z/\partial r = 0$ and $p = Re(r\omega)^2/2$.

In the stationary cylinder instance, ω and v_θ vanish identically. An outlet specification of pressure is necessary to remove the indeterminacy concerning the arbitrary level of pressure.

5. RESULTS AND DISCUSSION

Finite element results are presented for Newtonian and non-Newtonian flows. The viscous rheological parameterisation of expressions (3a–c) are used to model the non-Newtonian fluid properties. Models 1 and 3 have two adjustable parameters, *We* and *n*, whilst Model 2 has a single adjustable parameter *We*. Calculations are performed for different values of *We* ranging from 0 to 5, and *n* ranging from 0.3 to 1. For the stationary cylinder case, calculations are performed with Reynolds number ranging from 0 to 200. For rotating flow, all calculations are computed at $Re = 1$ and a rotation rate $\omega = 1$, i.e. $Ta = 0.25$. There are no theoretical solutions known for these constitutive models. Mesh refinement, together with comparison with numerical results from the literature, provide a check on the accuracy of present results. Rotating flows are denoted by a non-zero Taylor number *Ta*. In the field plots, the flow is upward past the sphere and ten equally spaced contours are shown between the maximum and the minimum value, with the exception of the streamfunction plots, in which case contours are more densely packed towards the centreline of the cylinder.

5.1. Newtonian drag

There is no closed form expression for the drag on a sphere falling through a cylindrical tube of Newtonian fluid. The most well-known approximate method for low Reynolds number flows was developed by Bohlin [7], who used a method of reflections. This formula is given in terms of a wall correction factor or drag coefficient, *K*, as follows

$$K \cong \left[1.0 - 2.10443\left(\frac{a}{R}\right) + 2.08877\left(\frac{a}{R}\right)^3 - 0.94813\left(\frac{a}{R}\right)^5 - 1.372\left(\frac{a}{R}\right)^6 + 3.87\left(\frac{a}{R}\right)^8 - 4.19\left(\frac{a}{R}\right)^{10} + \cdots \right]^{-1}. \tag{15}$$

Table III. Stokes drag coefficient for Newtonian flow, various a/R

a/R	Bohlin [7] reflection solution (15)	Haberman and Sayre [8] exact theory	Haberman and Sayre [8] solution (16)	Finite element results
0.1	1.2632	1.263	1.2633	1.2833
0.2	1.6794	1.680	1.6797	1.6792
0.3	2.3697	2.371	2.3697	2.3865
0.4	3.5884	3.596	3.5817	3.6083
0.5	5.9228	5.970	5.8700	5.9490
0.6	11.0566	11.135	10.5926	11.0453
0.7	(36.6017)	24.955	(21.4247	24.4812
0.8	(−11.7567)	73.555	(49.0229)	73.5048

Also, Haberman and Sayre [8] developed an approximate expression for the wall correction factor of the form

$$K = \left[1.0 - 0.75857\left(\frac{a}{R}\right)^5\right] \times \left[1.0 - 2.1050\left(\frac{a}{R}\right) + 2.0865\left(\frac{a}{R}\right)^3 - 1.7068\left(\frac{a}{R}\right)^5 + 0.72603\left(\frac{a}{R}\right)^6\right]^{-1}. \tag{16}$$

Rigorously, Equations (15) and (16) are valid only for $a/R \leq 0.6$. An exact solution for the Stokes drag coefficient is provided by Haberman and Sayre [8]. This was determined numerically as an approximate solution.

For $a/R = 0.1$–0.8, Table III provides a comparison of the finite element results with exact and approximate solutions of Haberman and Sayre, and the reflection solution of Bohlin. Values in parentheses are included for $a/R > 0.6$ for completeness and to illustrate the departure from the respective theoretical Equations (15) and (16), as they shift beyond their range of validity. A comparison with the experimental results of Fidleris and Whitmore [31] is shown in Figure 4, where there is good agreement, within $O(1\%)$. Against the finite element

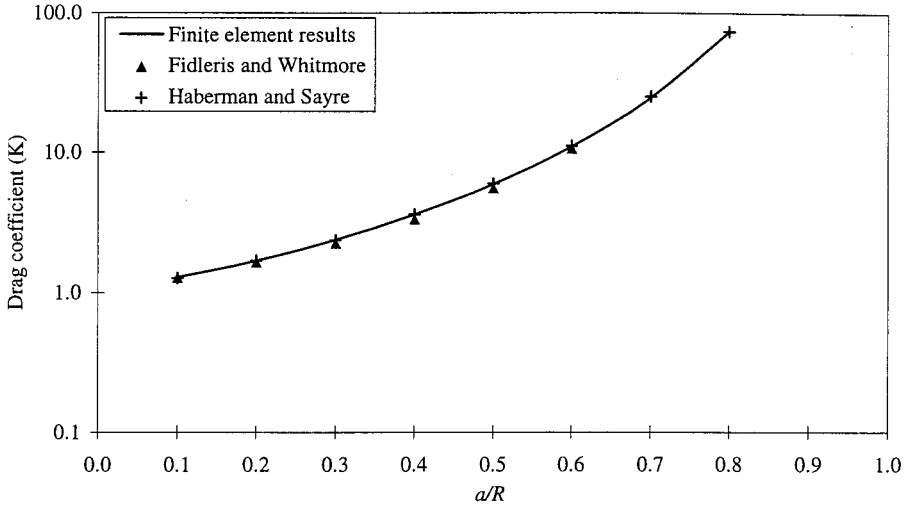

Figure 4. Stokes drag coefficient versus a/R.

Table IV. Stokes drag coefficient, $a/R = 0.5$

Literature	Technique	Drag coefficient
Harlen [34]	Boundary integral	5.9467
Luo and Tanner [35]	FEM	5.977
Crochet and Legal [36]	FEM	5.9475
Lunsmann *et al.* [37]	FEM	5.9474
Zheng *et al.* [38]	BEM	5.9466
Bohlin [7] reflection solution (15)	Reflection method	5.9228
Haberman and Sayre [8] exact theory	Exact theory	5.970
Haberman and Sayre [8] solution (16)	Approximate theory	5.8700
Present finite element result—M2 mesh	FEM	5.9490

results there is close agreement to $< 2\%$, with the solution of Bohlin up to $a/R = 0.6$, and the exact solution of Haberman and Sayre, which is also shown. The results of this study show good agreement with the numerical solutions of Carew and Townsend [32], Tullock *et al.* [33] and Harlen [34].

The geometric ratio $a/R = 0.5$ is selected as a benchmark for testing accuracy. The calculations in the Newtonian limit are assessed by comparison with the Stokes drag coefficient obtained by several independent techniques listed in Table IV. The finite element results find close agreement with those in the literature [34–38]. Note that the results of Luo and Tanner [35] and Haberman and Sayre [8] are quoted to three decimal places.

Solution convergence for Stokes flow with decreasing polar mesh size is confirmed in Table V for $a/R = 0.5$ with structured meshes, and $a/R = 0.2$ on unstructured meshes. Drag decreases for $a/R = 0.5$, yet increases for $a/R = 0.2$. On the basis of these results, meshes M2 and AM3 for the stationary cylinder case, and meshes M2 and AM2 for the rotating case are selected for further consideration.

Brenner and co-workers [10] provide a theoretical expression for pressure drop on a falling sphere settling in a long cylinder for Stokes and Oseen regimes as

$$\frac{(\Delta P)A_c}{D} = 2\left[1 - \frac{2}{3}\left(\frac{a}{R}\right)^2\right] + O\left(\frac{a}{R}\right)^3. \tag{17}$$

Here, ΔP is the pressure drop created by the motion of the sphere settling along the axis and A_c is the cylinder cross-sectional area. The pressure drop to force–drag ratio predicted by the finite element simulations for Stokes flow, with $a/R = 0.5$ and 0.2, is 1.6685 (on M2 mesh) and 1.9470 (on AM3 mesh), respectively. This is noted to be within $O(0.1)\%$ and less than that of Equation (17), which provides comparable values of 1.6667 for $a/R = 0.5$ and 1.9467 for $a/R = 0.2$.

Table V. Stokes drag coefficient, convergence with decreasing polar mesh size

Mesh	Mesh size on sphere	Drag coefficient
M1 ($a/R = 0.5$)	0.1428	5.9930
M2 ($a/R = 0.5$)	0.0748	5.9490
M4 ($a/R = 0.5$)	0.0383	5.9405
AM1 ($a/R = 0.2$)	0.1428	1.6651
AM2 ($a/R = 0.2$)	0.0748	1.6751
AM3 ($a/R = 0.2$)	0.0383	1.6792

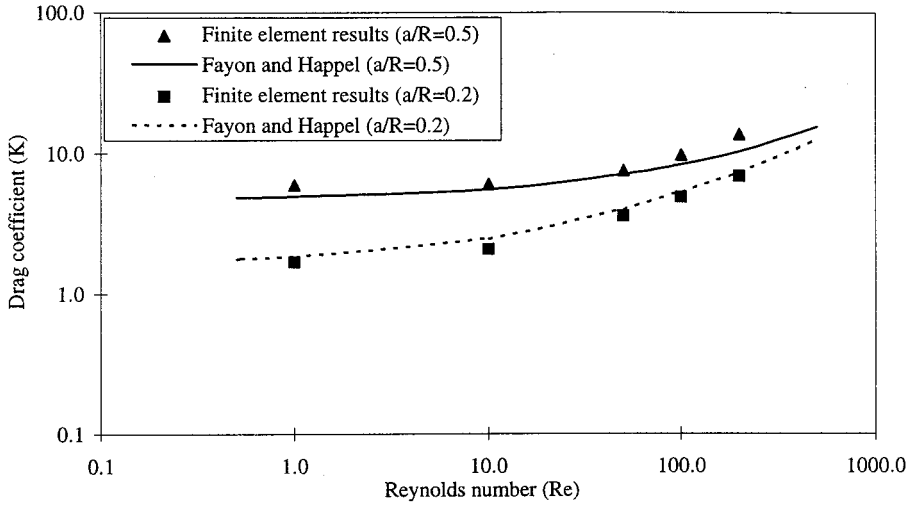

Figure 5. Newtonian drag coefficient versus *Re*.

Fayon and Happel [9] obtained a semi-empirical equation for the drag coefficient in terms of Reynolds number for Newtonian flow as

$$K = \left\{ \left[1 - 2.105\left(\frac{a}{R}\right) + 2.087\left(\frac{a}{R}\right)^3 \right]^{-1} + \left(\frac{C_\infty}{C_S} - 1\right) \right\}, \tag{18}$$

where $C_s = 24/Re$ is the drag coefficient according to Stokes law, and C_∞ is the drag coefficient in an unbounded medium. Experimental data for C_∞ were taken from Perry [39]. Figure 5 provides a log–log plot comparison of Newtonian finite element predictions with the semi-empirical calculations borne out of Equation (18), displaying close correlation throughout the range of *Re*, with rising drag coefficient for increasing Reynolds number.

For the bounded rotating flow problem, there are no known theoretical or approximate expressions for the drag coefficient. It is observed from Table VI, that the drag experienced by a sphere falling in a rotating fluid is slightly greater than that experienced in a non-rotating fluid. Similar behaviour is observed in the experimental results of Maxworthy [20], and the numerical calculations of Dennis *et al.* [26] for unbounded low Reynolds number flow, i.e. $Re \leq 1$.

Table VI. Newtonian drag coefficient, $a/R = 0.5$ and 0.2, $Re = 1$

Mesh	Drag coefficient non-rotating flow	Drag coefficient rotating flow ($Ta = 0.25$)
M2 ($a/R = 0.5$)	5.9504	5.9511
AM1 ($a/R = 0.2$)	1.6734	1.6911
AM2 ($a/R = 0.2$)	1.6837	1.6988
AM3 ($a/R = 0.2$)	1.6876	1.7005

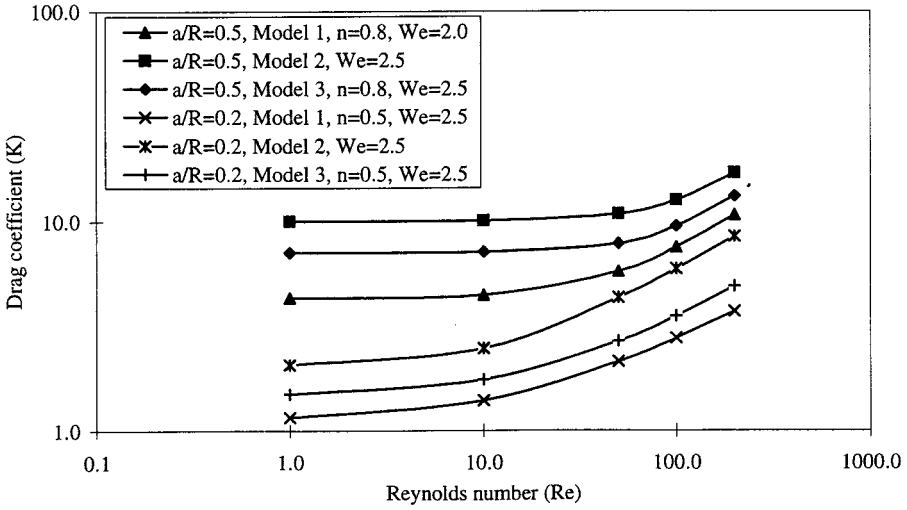

Figure 6. Drag coefficient of non-Newtonian fluid versus *Re*.

5.2. Non-Newtonian drag

Figure 6 compares the drag coefficient for different Reynolds numbers for non-rotating flow for $a/R = 0.5$ and 0.2. In all cases, drag enhancement is observed with increasing Reynolds number in this log–log plot. Drag enhancement is more prominent for the $a/R = 0.2$ case. For $a/R = 0.5$, the drag increases marginally for Reynolds number up to ten in this log–log plot, and then increases more substantially for $Re > 10$. Similar results are observed in Figure 5 for Newtonian fluids. Drag coefficient values for Model 3, lie between those for Models 1 and 2, reflecting the combined effects of shear-thinning and extension-thickening.

Figures 7 and 8 display drag coefficient trends with variation in the power-law index n for Models 1 and 3. Decreasing n, whilst amplifying shear-thinning, spawns drag reduction. For

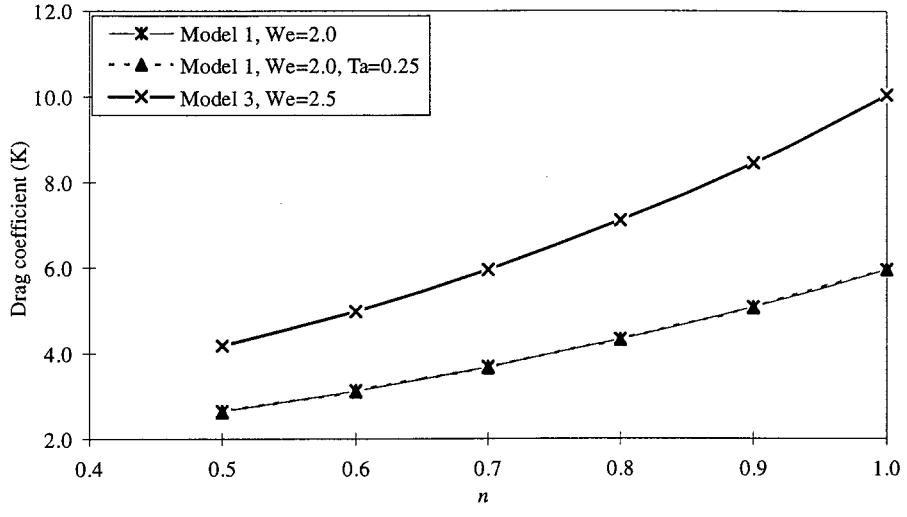

Figure 7. Drag coefficient versus power-law index n: $a/R = 0.5$ and $Re = 1$.

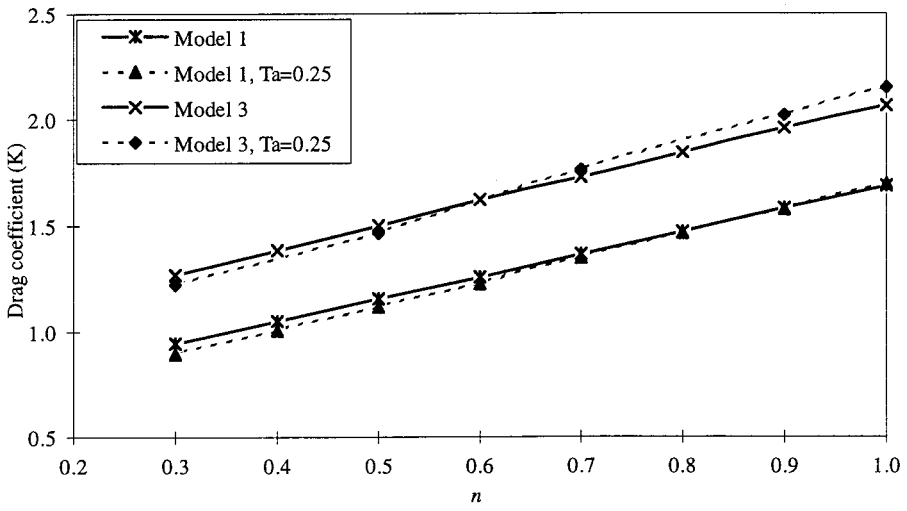

Figure 8. Drag coefficient versus power-law index n: $a/R = 0.2$, $We = 2.5$ and $Re = 1$.

$a/R = 0.2$, a linear dependency on n emerges. For lower values of n, rotating flow generates less drag than that for non-rotating flow; a trend that is reversed for larger values of n. The additional extension-thickening behaviour supported by Model 3 over Model 1, gives rise to a uniform elevation in drag across the range of n.

Calculations have been conducted for all three models for $0 \leq We \leq 5$. The variation of drag coefficient with increasing We is charted in Figures 9 and 10 for $a/R = 0.5$ and 0.2, respectively. For Model 1, increased shear-thinning provides drag reduction. For Model 2, increasing extension-thickening stimulates drag enhancement. The drag in rotating flow is observed to be larger than that for the non-rotating case, rotation giving rise to increased extension-thickening. The finite element predictions for $a/R = 0.5$ and non-rotating flow correspond closely with the earlier investigation of Debbaut and Crochet [6]. For Model 3, the drag coefficient first decreases to a minimum before increasing. This response is due to the

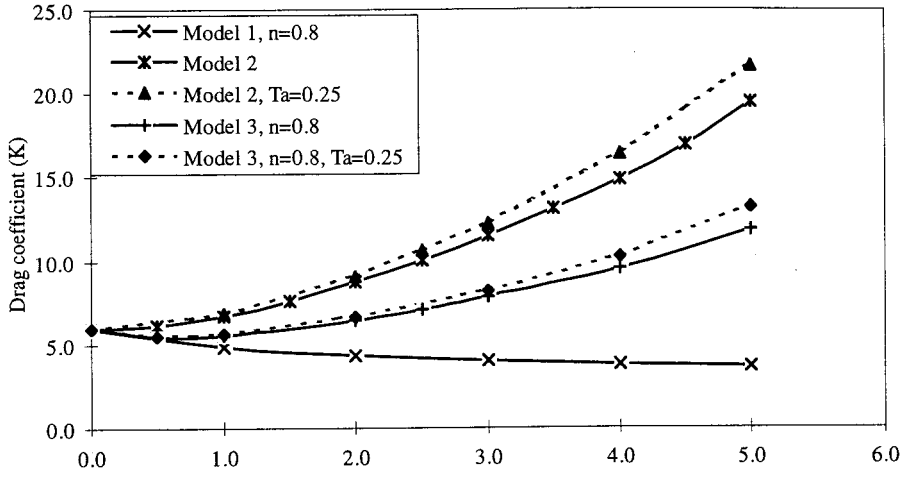

Figure 9. Drag coefficient versus We: $a/R = 0.5$ and $Re = 1$.

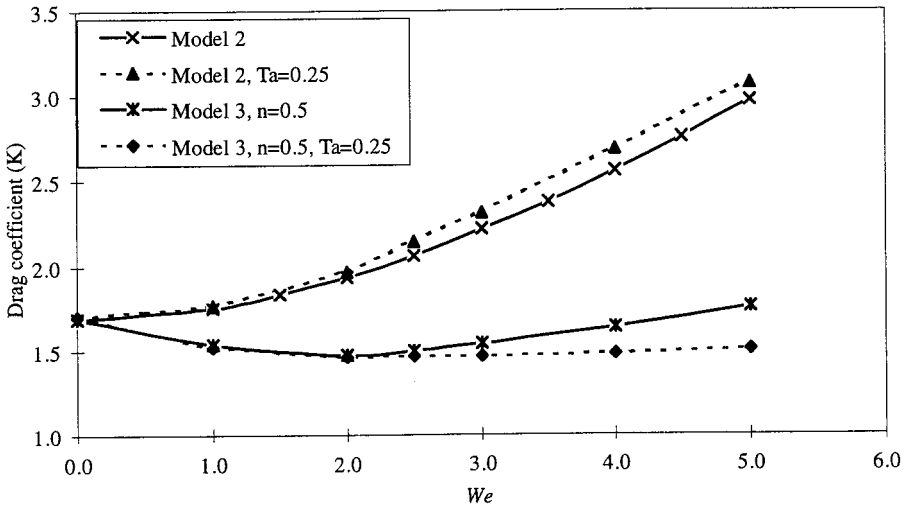

Figure 10. Drag coefficient versus We: $a/R = 0.2$ and $Re = 1$.

initial domination of the shear-thinning properties of the model, prior to supression by extension-thickening behaviour. The early dip in drag is more pronounced and persists over a larger range of We at the wider gap setting of $a/R = 0.2$ and lower value of $n = 0.5$. This is attributed to the change in n by inspection from Figures 7 and 8. For $a/R = 0.5$ and $n = 0.8$, the drag coefficient for the rotating flow exceeds that for the non-rotating case; the converse is true for $a/R = 0.2$ and $n = 0.5$. This is due to increased shear-thinning effects in the rotating flow with decrease in n, as observed in Figures 7 and 8.

Table VII. Drag coefficient, convergence with decreasing polar mesh size, non-rotating flow: Model 3, $a/R = 0.2$, $n = 0.5$ and $Re = 1$

We	Mesh-AM1	Mesh-AM2	Mesh-AM3
0.0	1.6733	1.6833	1.6876
1.0	1.5192	1.5311	1.5348
2.0	1.4606	1.4782	1.4818
3.0	1.4952	1.5301	1.5407
4.0	1.5702	1.6144	1.6384
5.0	1.6642	1.7117	1.7568

Table VIII. Drag coefficient, convergence with decreasing polar mesh size, rotating flow: Model 3, $a/R = 0.1$, $n = 0.5$, $Re = 1$ and $Ta = 0.25$

We	Mesh-AM1	Mesh-AM2
0.0	1.6911	1.6988
1.0	1.5057	1.5147
2.0	1.4474	1.4579
3.0	1.4399	1.4509
4.0	1.4499	1.4566
5.0	1.4522	1.4612

The computed values of the drag coefficient as a function of We are shown in Tables VII and VIII for Model 3 and $a/R = 0.2$. These results are calculated with unstructured meshes of AM1, AM2 and AM3 for non-rotating flow, and meshes of AM1 and AM2 for rotating flow. With decreasing polar mesh size, the results for each mesh show an initial decrease in drag coefficient followed by an increase, confirming adequate convergence trends with mesh refinement.

When the sphere–cylinder gap is reduced, the results shown in Figures 6–10 indicate that shear-thinning, extension-thickening and shear-thinning combined with extension-thickening, can have a significant enhancing effect on the drag. This is due to the rapid decrease in the degree of extension-thickening and shear-thinning as the ratio a/R diminishes, corresponding to a widening of the gap.

5.3. Flow field

Qualitative changes in the flow field give rise to variation in the drag coefficient. For the geometric ratio $a/R = 0.2$, the influence of inertia and rotation on the flow field are examined separately. Contours of streamfunction, velocity, stress, pressure and viscosity for Model 3 are shown in Figures 11–13 at parameter settings of $n = 0.5$ and $We = 2.5$. Contour extrema are provided in Table IX, where levels are taken at equal increments. In all cases, the flow accelerates as the fluid approaches the sphere.

In non-rotating flow, as displayed in Figures 11 and 12 where Re increases from 1 to 100, the increase in vortex length and intensity with inertia is clear. For $Re = 100$, thin radial velocity boundary layers develop adjacent to the sphere surface on the upstream side, and changes in axial velocity are protracted a long distance downstream of the sphere. Pressure extrema appear on the upstream and downstream surface of the sphere at $Re = 1$. As Reynolds number increases, the separation line shifts downstream, so that the attached recirculating wake widens and lengthens. Therefore, the position of the minimum pressure point moves upstream as Re increases from 1 to 100, with attendant changes in the stress field. Normal stresses at $Re = 1$, develop thin boundary layers near the upstream and downstream stagnation points. At the larger value of $Re = 100$, a steep normal stress boundary layer develops near the sphere surface over the upstream portion. Shear stress at $Re = 1$, develops lateral boundary layers around either side of the sphere. For $Re = 100$, the increased level of inertia produces an upstream shift in the shear stress boundary layer, that significantly modifies the viscosity field near the sphere surface.

At $Re = 1$, adjustment of streamline patterns is minor between non-rotating and rotating flows. For the rotating case, the downstream azimuthal velocity is shifted more toward the sphere surface. Only the fields that stand apart from the non-rotating case are displayed in Figure 13.

6. CONCLUSIONS

This study has provided a particular instance of a testing practical engineering application to demonstrate the scope and power of the numerical procedure employed. The now well-established performance of the numerical technique covers a wide range of flow situations and applications, covering classical benchmark problems to industrial complex flows providing validation for the implementation. This includes examples of flows in two and three dimen-

sions [40–42], steady and unsteady conditions [43,44], isothermal and non-isothermal conditions [45,46] for fibre suspensions [50], and Newtonian, inelastic [49] and viscoelastic materials [47,48]. Industrial applications addressed include injection moulding [51] and wire-coating [52] processes dealing with polymer melt flows.

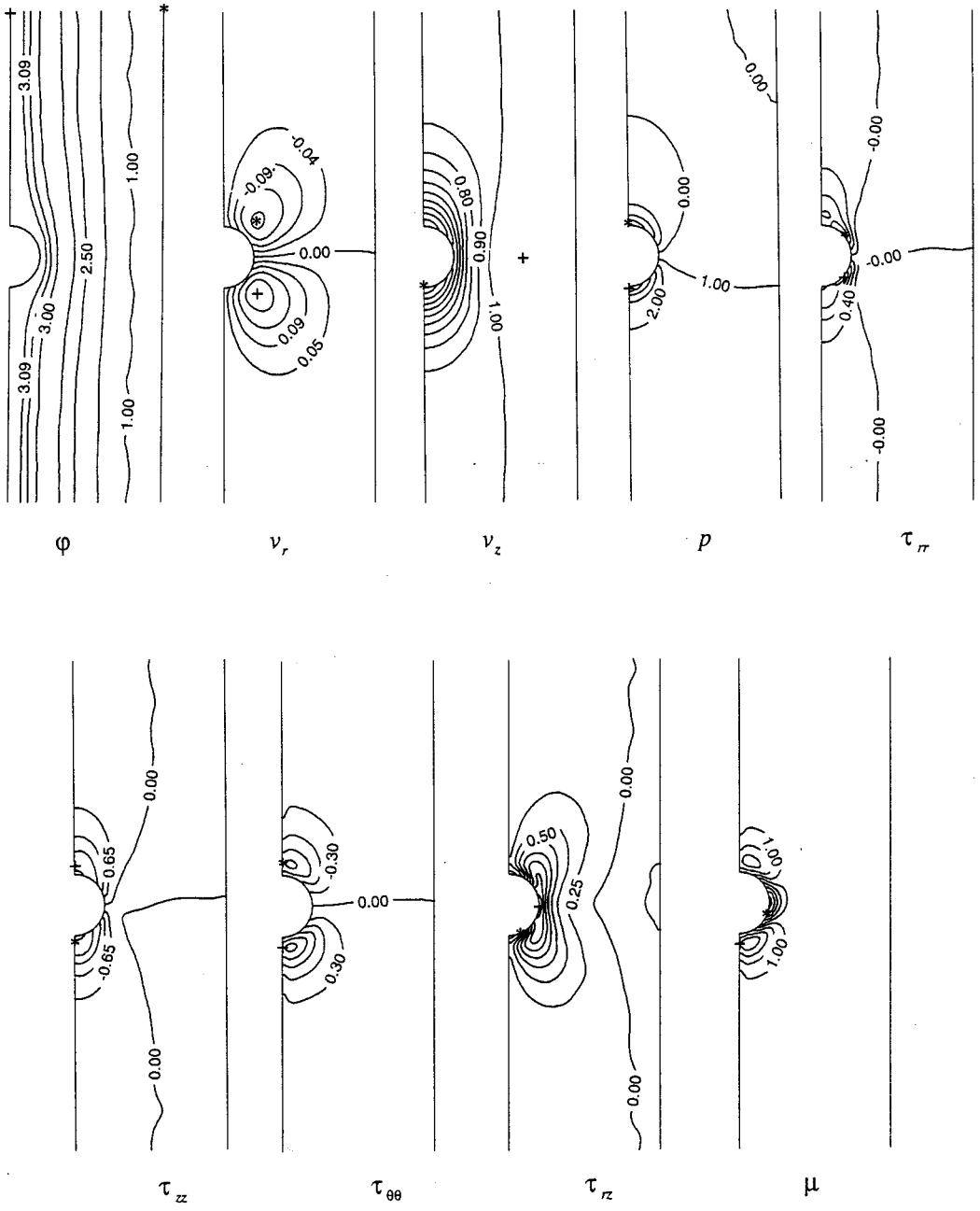

Figure 11. Contours of streamfunction (φ), radial velocity (v_r), axial velocity (v_z), pressure (p), stress components (τ_{rr}, τ_{zz}, $\tau_{\theta\theta}$, τ_{rz}) and viscosity (μ); Model 3: $a/R = 0.2$, $Re = 1$, $We = 2.5$ and $n = 0.5$.

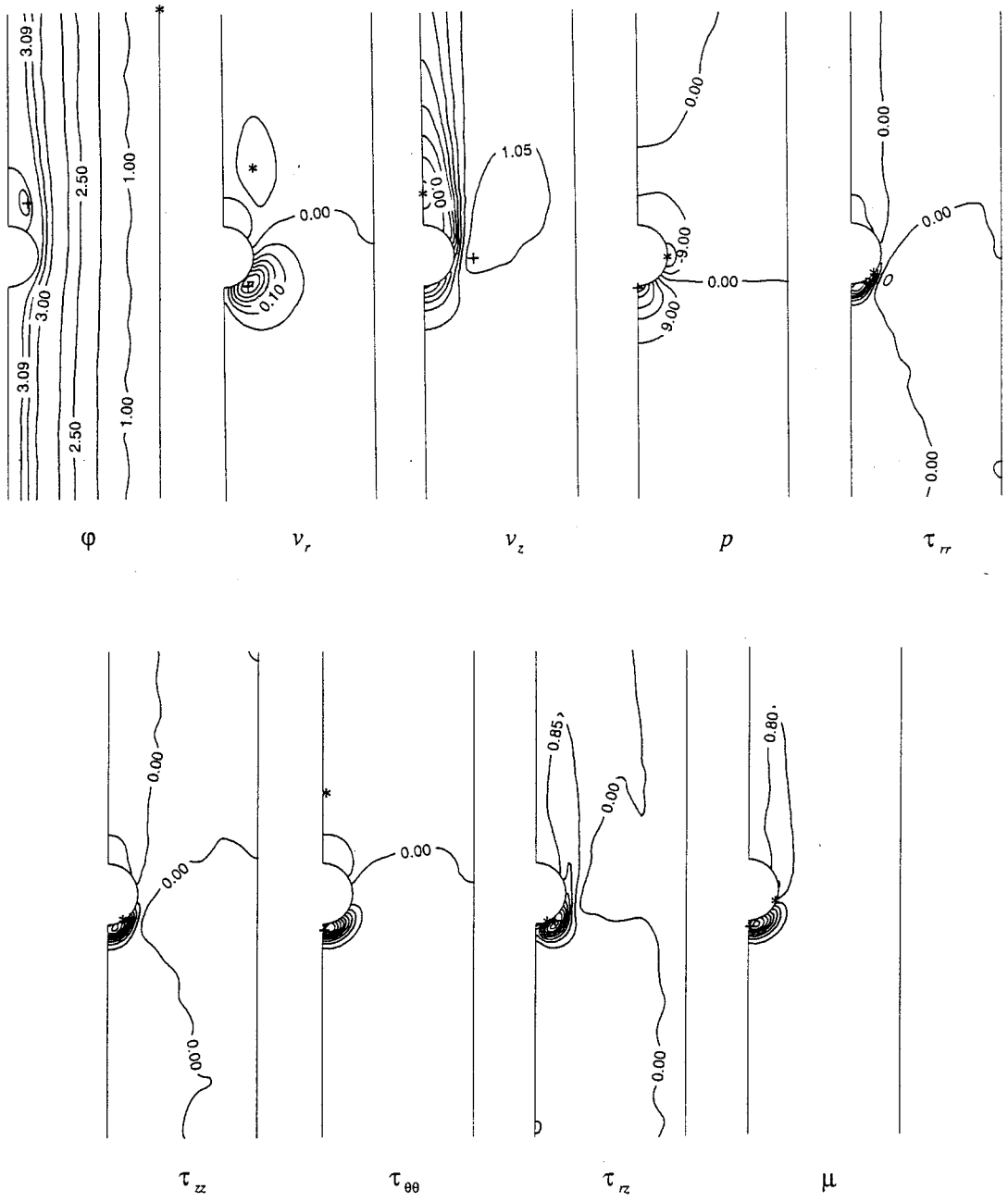

Figure 12. Contours of streamfunction (φ), radial velocity (v_r), axial velocity (v_z), pressure (p), stress components (τ_{rr}, τ_{zz}, $\tau_{\theta\theta}$, τ_{rz}) and viscosity (μ); Model 3: $a/R = 0.2$, $Re = 100$, $We = 2.5$ and $n = 0.5$.

The main conclusions for this settling flow case study may be summarised as follows. For the stationary cylinder instance, accurate results are derived for the Stokes drag coefficient at eight different sphere to cylinder radius ratios between 0.1 and 0.8. *Increasing inertia* causes drag enhancement for Newtonian and non-Newtonian models alike. Drag coefficient values for

Model 3, lie between those for Models 1 and 2, reflecting the combined effects of shear-thinning and extension-thickening. To demonstrate the effect of rotation, comparisons have been performed at $Re = 1$ and for rotating flow with $Ta = 0.25$. For the Newtonian problem, drag coefficient for rotating flow is slightly greater than that in its non-rotating counterpart.

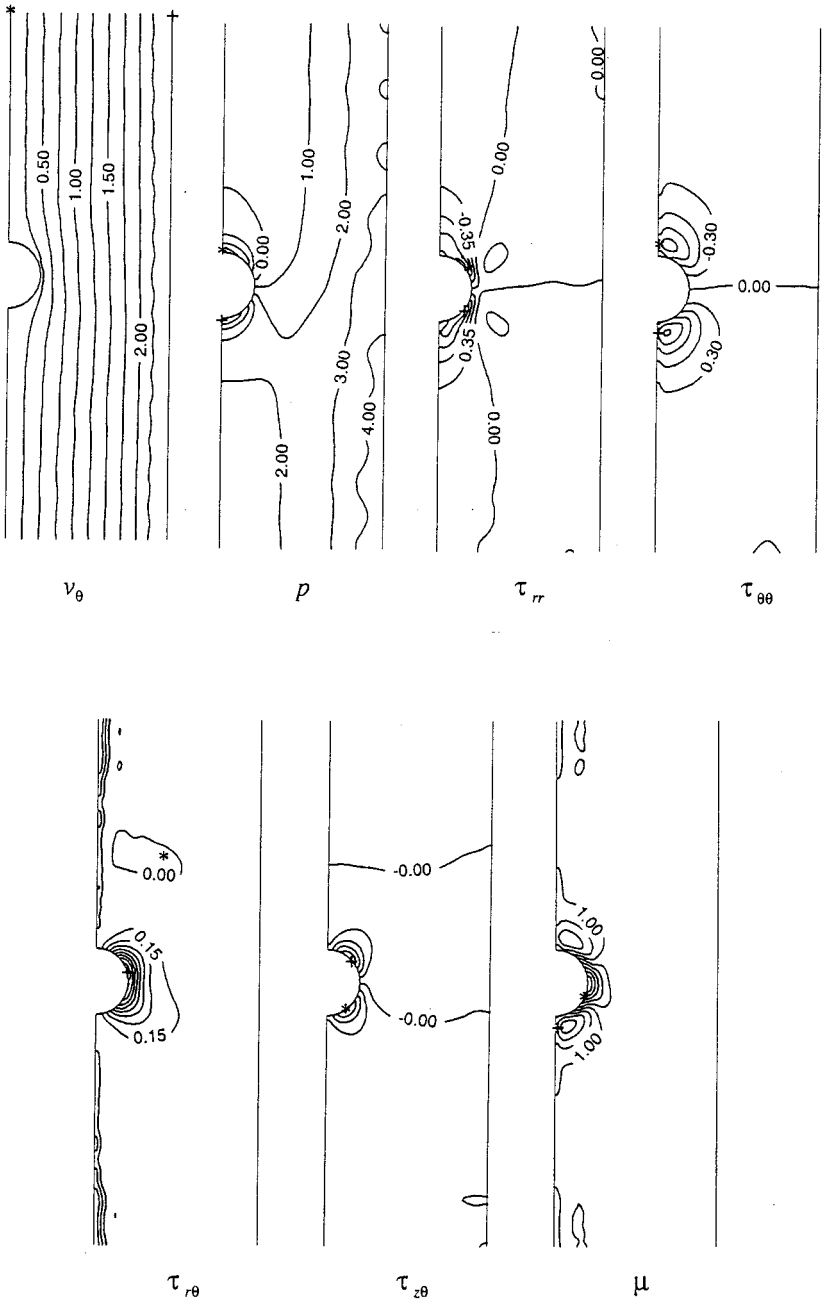

Figure 13. Contours of azimuthal velocity (v_θ), pressure (p), stress components (τ_{rr}, $\tau_{\theta\theta}$, $\tau_{r\theta}$, $\tau_{z\theta}$) and viscosity (μ); Model 3: $a/R = 0.2$, $Re = 1$, $Ta = 0.25$, $We = 2.5$ and $n = 0.5$.

Table IX. Extrema contour levels for Figures 11–13: Model 3, $a/R = 0.2$, $We = 2.5$ and $n = 0.5$

Flow field	Figure 11 $Re = 1$		Figure 12 $Re = 100$		Figure 13 $Re = 1$, $Ta = 0.25$	
	Min. (*)	Max. (+)	Min. (*)	Max. (+)	Min. (*)	Max (+)
φ	0.0000	31.250	0.0000	3.1298	–	–
v_r	−0.1933	0.2171	−0.0918	0.3897	–	–
v_θ	–	–	–	–	0.0000	2.5000
v_z	0.0000	1.1249	−0.1977	1.1165	–	–
p	−4.9296	7.8010	−26.617	104.44	−5.0847	8.0708
τ_{rr}	−2.6545	3.1418	−8.7756	37.403	−2.8200	2.8309
τ_{zz}	−3.6693	2.8291	−41.467	3.0184	–	–
$\tau_{\theta\theta}$	−1.4139	1.8356	−0.4326	19.969	−1.5050	1.7803
τ_{rz}	−1.3276	2.9703	−17.422	17.181	–	–
$\tau_{r\theta}$	–	–	–	–	−0.0036	1.9128
$\tau_{z\theta}$	–	–	–	–	−1.3233	1.5293
μ	0.2444	1.4672	0.1051	7.6491	0.2331	1.4460

With decreasing power-law index, drag decreases monotonically for Model 1, a shear-thinning fluid. At a wider gap setting of $a/R = 0.2$, drag is linearly dependent on n. Drag for rotating flow is slightly greater than that for the non-rotating case at larger values of n; a trend reversed at lower values of n. The additional extension-thickening, supported by Model 3 over Model 1, gives rise to an elevation in drag uniformly across the range of n.

Influence of variation of drag coefficient *with increasing We* may be summarised as follows. For Model 1, increased shear-thinning provides drag reduction. Alternatively, for Model 2, an extension-thickening fluid, drag enhancement is observed. This is true in both rotating and non-rotating instances, with the larger drag emerging for rotating flow. For Model 3, a combined shear-thinning and extension-thickening fluid, the drag first decreases to a minimum, whilst shear-thinning dominates, before rising as extension-thickening takes over at larger values of We. For $a/R = 0.5$ and $n = 0.8$, the drag for the rotating flow exceeds that for the non-rotating instance, the situation being reversed for $a/R = 0.2$ and $n = 0.5$. This is due to increased shear-thinning effects in the rotating flow with decreasing n.

In general for Model 3, the *flow field* is influenced more significantly by the introduction of inertia than rotation. At a fixed unitary level of inertia, there are hardly any visible differences in flow field between rotating and non-rotating instances. Likewise, in this respect, Models 1 and 2 display similar qualitative flow field structure to that described for Model 3.

REFERENCES

1. R. Clift, J.R. Grace and M.E. Weber, *Bubbles, Drops and Particles*, Academic Press, New York, 1978.
2. J. Happel and H. Brenner, *Low Reynolds Number Hydrodynamics*, Martinus Nijhoff Publishers, The Hague, 1983.
3. R.P. Chhabra, *Bubbles, Drops and Particles in non-Newtonian Fluids*, CRC Press, Boca Raton, 1993.
4. R.B. Bird, R.C. Armstrong and O. Hassager, *Dynamics of Polymeric Liquids*, Vol. 1, 2nd edn., Wiley, New York, 1987.
5. C.J.S. Petrie, *Elongational Flows*, Pitman, London, 1979.
6. B. Debbaut and M.J. Crochet, 'Extensional effects in complex flows', *J. Non-Newtonian Fluid Mech.*, **30**, 169–184 (1988).
7. T. Bohlin, 'On the drag on a rigid sphere moving in a viscous fluid inside a cylindrical tube', *Trans. Roy. Inst. Technol.* (Stockholm), No. 155, (1960).

8. W.L. Haberman and R.M. Sayre, 'Motion of rigid and fluid spheres in stationary and moving liquids inside cylindrical tubes', *Hydromechanics laboratory*, *Research and development report No.1143*, Department of the Navy, David Taylor Model Basin, 1958.
9. A.M. Fayon and J. Happel, 'Effects of a cylindrical boundary on a fixed rigid sphere in a moving viscous fluid', *AIChE J.*, **6**, 55–58 (1960).
10. G.A. Feldman and H. Brenner, 'Experiments on the pressure drop created by a sphere settling in a viscous liquid, Part 2, Reynolds numbers from 0.2 to 21 000', *J. Fluid Mech.*, **32**, 705–720 (1968).
11. Y. Kawase and M. Moo-Young, 'Approximate solutions for power-law fluid flow past a particle at low Reynolds numbers', *J. Non-Newtonian Fluid Mech.*, **21**, 167–177 (1986).
12. J.H. Oh and S.J. Lee, 'A rheological study on viscoelastic flow past spheres in a cylinder', *J. Mater. Proc. Manuf. Sci.*, **1**, 3–15 (1992).
13. R.P. Chhabra and P.H.T. Uhlherr, 'Wall effect for high Reynolds number motion of spheres in shear-thinning fluids', *Chem. Eng. Commun.*, **5**, 115–124 (1980).
14. Gu Dazhi and R.I. Tanner, 'The drag on a sphere in a power-law fluid', *J. Non-Newtonian Fluid Mech.*, **17**, 1–12 (1985).
15. D.I. Graham and T.E.R. Jones, 'Settling and transport of spherical particles in power-law fluids at finite Reynolds number', *J. Non-Newtonian Fluid Mech.*, **54**, 465–488 (1994).
16. M.B. Bush and N. Phan-Thien, 'Drag force on a sphere in creeping motion through a Carreau model fluid', *J. Non-Newtonian Fluid Mech.*, **16**, 303–313 (1984).
17. R. Zheng, N. Phan-Thien and R.I. Tanner, 'The flow past a sphere in a cylindrical tube: effects of inertia, shear-thinning and elasticity', *Rheol. Acta*, **30**, 499–510 (1991).
18. G.I. Taylor, 'The motion of a sphere in a rotating liquid', *Proc. Roy. Soc. Lond. A*, **102**, 180–189 (1922).
19. W.G. Pritchard, 'The motion generated by a body moving along the axis of a uniformly rotating fluid', *J. Fluid Mech.*, **39**, 443–464 (1969).
20. T. Maxworthy, 'An experimental determination of the slow motion of a sphere in a rotating, viscous fluid', *J. Fluid Mech.*, **23**, 373–384 (1965).
21. S.F. Grace, 'On the motion of a sphere in a rotating liquid', *Proc. R. Soc. Lond. A*, **113**, 46–77 (1926).
22. K. Stewartson, 'On the motion of a sphere along the axis of a rotating fluid', *Q. J. Mech. Appl. Math.*, **11**, 39–51 (1958).
23. S. Childress, 'The slow motion of a sphere in a rotating, viscous fluid', *J. Fluid Mech.*, **20**, 305–314 (1964).
24. A.J. Weisenborn, 'Drag on a sphere moving slowly in a rotating viscous fluid', *J. Fluid Mech.*, **153**, 215–227 (1985).
25. J.P. Tanzosh and H.A. Stone, 'Motion of a rigid particle in a rotating viscous flow: an integral equations approach', *J. Fluid Mech.*, **275**, 225–256 (1994).
26. S.C.R. Dennis, D.B. Ingham and S.N. Singh, 'The slow translation of a sphere in a rotating viscous fluid', *J. Fluid Mech.*, **117**, 251–267 (1982).
27. D.M. Hawken, H.R. Tamaddon-Jahromi, P. Townsend and M.F. Webster, 'A Taylor–Galerkin-based algorithm for viscous incompressible flow', *Int. j. numer. methods fluids*, **10**, 327–351 (1990).
28. P.R. Schunk and L.E. Scriven, 'Constitutive equation for modeling mixed extension and shear in polymer solution processing', *J. Rheol.*, **34**, 1085–1119 (1990).
29. N.D. Levine, 'Superconvergent recovery of the gradient from piecewise linear finite element approximations', *IMA J. Numer. Anal.*, **5**, 407–427 (1985).
30. D.M. Hawken, P. Townsend and M.F. Webster, 'A comparison of gradient recovery methods in finite-element calculations', *Commun. Appl. Numer. Methods*, **7**, 195–204 (1991).
31. V. Fidleris and R.L. Whitmore, 'Experimental determination of the wall effect for spheres falling axially in cylindrical vessels', *Br. J. Appl. Phys.*, **12**, 490–494 (1961).
32. E.O.A. Carew and P. Townsend, 'Non-Newtonian flow past a sphere in a long cylindrical tube', *Rheol. Acta*, **27**, 125–129 (1988).
33. D.L. Tullock, N. Phan-Thien and A.L. Graham, 'Boundary element simulations of spheres settling in circular, square and triangular conduits', *Rheol. Acta*, **31**, 139–150 (1992).
34. O.G. Harlen, 'High-Deborah-Number flow of a dilute polymer solution past a sphere falling along the axis of a cylindrical tube', *J. Non-Newtonian Fluid Mech.*, **37**, 157–173 (1990).
35. X.L. Luo and R.I. Tanner, 'A streamline element scheme for solving viscoelastic flow problems, Part 1. Differential constitutive equations', *J. Non-Newtonian Fluid Mech.*, **21**, 179–199 (1986).
36. M.J. Crochet and V. Legat, 'The consistent streamline-upwind/Petrov-Galerkin method for viscoelastic flow revisited', *J. Non-Newtonian Fluid Mech.*, **42**, 283–299 (1992).
37. W.J. Lunsmann, L. Genieser, R.C. Armstrong and R.A. Brown, 'Finite element analysis of steady viscoelastic flow around a sphere in a tube: calculations with constant viscosity models', *J. Non-Newtonian Fluid Mech.*, **48**, 63–99 (1993).
38. R. Zheng, N. Phan-Thien and R.I. Tanner, 'On the flow past a sphere in a cylindrical tube: limiting Weissenberg number', *J. Non-Newtonian Fluid Mech.*, **36**, 27–49 (1990).
39. J.H. Perry, *Chemical Engineers' Handbook*, Vol. 4, R.H. Perry, C.H. Chilton and S.D. Kirkpatrick (eds.), McGraw-Hill, New York, 1963, pp. 5–61.

40. D.M. Hawken, P. Townsend and M.F. Webster, 'Numerical simulation of viscous flows in channels with a step', *J. Comput. Fluids*, **20**, 59–75 (1991).
41. O. Hassager, P. Henriksen, P. Townsend, M.F. Webster and D. Ding, 'The quarterbend: a three-dimensional benchmark problem', *J. Comput. Fluids*, **20**, 373–386 (1991).
42. A. Baloch, P. Townsend and M.F. Webster, 'On two and three dimensional expansion flows', *J. Comput. Fluids*, **24**, 863–882 (1995).
43. H.R. Tamaddon-Jahromi, P. Townsend and M.F. Webster, 'Flow past a cylinder with and without an appurtenance', *Int. j. numer. methods eng.*, **36**, 3991–4008 (1993).
44. H.R. Tamaddon-Jahromi, P. Townsend and M.F. Webster, 'Unsteady viscous flow past a flat plate orthogonal to the flow', *J. Comput. Fluids*, **23**, 433–446 (1994).
45. D. Ding, P. Townsend and M.F. Webster, 'On computation of two and three-dimensional unsteady thermal non-Newtonian flows', *Int. J. Numer. Methods Heat Fluid Flow*, **5**, 495–510 (1995).
46. D. Ding, P. Townsend and M.F. Webster, 'Computer modelling of transient thermal flows of non-Newtonian Fluids', *J. Non-Newtonian Fluid Mech.*, **47**, 239–265 (1993).
47. A. Baloch, P. Townsend and M.F. Webster, 'On vortex development in viscoelastic expansion and contraction flows', *J. Non-Newtonian Fluid Mech.*, **65**, 133–149 (1996).
48. S. Gunter, P. Townsend and M.F. Webster, 'Simulation of some model viscoelastic extensional flows', *Int. j. numer. methods fluids*, **23**, 691–710 (1996).
49. A. Baloch, P. Townsend and M.F. Webster, 'Extensional effects in flows through contractions with abrupt or rounded corners', *J. Non-Newtonian Fluid Mech.*, **54**, 285–302 (1994).
50. A. Baloch and M.F. Webster, 'A computer simulation of complex flows of fibre suspensions', *J. Comput. Fluids*, **24**, 135–151 (1995).
51. G.J. Manogg, P.Townsend and M.F. Webster, 'Numerical simulation of multilayer injection moulding', *J. Non-Newtonian Fluid Mech.*, **68**, 153–167 (1997).
52. S. Gunter, P. Townsend, M.F. Webster, D. Binding, A. Blythe and A. Mosquera, 'Modelling polymer melt flows in wirecoating processes', *J. Non-Newtonian Fluid Mech.*, **64**, 191–206 (1996).

